8 Jun 87   Conference Presentation

Forced Unsteady Vortex Flows   TA 2307-F1-38
Driven by Pitching Airfoils

J.M. Walker, D.C. Chou

F.J. Seiler Research Laboratory   FJSRL-PR-90-0007
USAF Academy CO 80840-6528

DTIC
ELECTE
OCT 31 1990
E   D

Distribution Unlimited

Experiments were conducted with a NACA 0015 airfoil pitching rapidly to high angles of attack to study the initiation, development, and evolution of dynamic stall vortex flows. The airfoil was pitched about its quarter-chord axis from zero to 60 degrees geometric angle of attack at rates from 115 deg/sec to 1380 deg/sec and at flow speeds from 10 to 80 ft/sec (chord Reynolds numbers from 25,000 to 200,000). Smoke-wire flow visualization, dynamic surface velocity magnitude measurement experiments were performed and correlated to determine the nature of the elicited time dependent vortex flows. Lift, pressure drag, and moment coefficients were calculated to be far in excess of the maximum steady flow values and were shown to be functions of the non-dimensional pitch rate.

flow visualization   13
dynamic loads
vortices

UNCLASSIFIED   UNCLASSIFIED   UNCLASSIFIED   NONE

AIAA-87-1331

Forced Unsteady Vortex Flows Driven by Pitching Airfoils

J. M. Walker, Frank J. Seiler

Research Laboratory, USAF Academy, CO

D. C. Chou, Dept. of Mechanical Engineering,

University of New Mexico, Albuquerque, NM

AIAA 19th Fluid Dynamics, Plasma Dynamics and Lasers Conference

June 8-10, 1987/Honolulu, Hawaii

FORCED UNSTEADY VORTEX FLOWS
DRIVEN BY PITCHING AIRFOILS

John M. Walker*
Frank J. Seiler Research Laboratory
USAF Academy, Colorado Springs, CO 80840-6528

David C. Chou**
Department of Mechanical Engineering
University of New Mexico, Albuquerque, NM 87131

Abstract

Experiments were conducted with a NACA 0015 airfoil pitching rapidly to high angles of attack to study the initiation, development, and evolution of dynamic stall vortex flows. The airfoil was pitched about its quarter-chord axis from zero to sixty degrees geometric angle of attack at rates from 115 deg/sec to 1380 deg/sec and at flow speeds from 10 to 80 ft/sec (chord Reynolds numbers from 25,000 to 200,000). Smoke-wire flow visualization, dynamic surface pressure measurement, and near-surface hot-film velocity magnitude measurement experiments were performed and correlated to determine the nature of the elicited time dependent vortex flows. Lift, pressure drag, and moment coefficients were calculated to be far in excess of the maximum steady flow values and were shown to be functions of the non-dimensional pitch rate.

Nomenclature

c	Airfoil chord
c_d	Airfoil pressure drag coefficient
c_ℓ	Airfoil lift coefficient
$c_{mc/4}$	Airfoil 1/4 c moment coefficient
c_p	Airfoil pressure coefficient
Re	Chord Reynolds number $= U_\infty c/\nu$
t	Time
U_∞	Freestream velocity
$\dot\alpha$	Pitch rate
α^+	Non-dimensional pitch rate $= \dot\alpha c/U_\infty$
ν	Kinematic viscosity

Introduction

Unsteady aerodynamics has been a topic of interest[1] for most of this century. But only in the last two decades has computer technology become adequate for computational and experimental studies of transient aerodynamic phenomena. Recently, forced unsteady separated flows[2] have received added emphasis. This interest has evolved from the first studies of dynamic overshoot[3] in lift on helicopter rotors. A number of experimental studies[4,5,6,7] have been performed on low amplitude oscillating airfoils to study this effect, and subsequent analytical studies[2,8,9] have attempted to explain the phenomenon. Only a few efforts[10,11,12,13] have been directed toward high amplitude, high rate motions. The latter studies have been motivated by a desire to exploit the large aerodynamic forces generated by these motions for enhanced aircraft maneuverability.

The experimental investigations reported herein were performed in an attempt to examine the extremes of large transient aerodynamic forces generated by forced unsteady flows, to quantify the important parameters affecting these flows, and to obtain a better understanding of the mechanisms involved in producing them.

Methods

These experiments were conducted in both the 2 ft x 3 ft subsonic wind tunnel at the Aeronautics Laboratory at the U.S. Air Force Academy and the low turbulence 2 ft x 2 ft low speed wind tunnel at the University of Colorado, Boulder. The airfoil models were full span NACA 0015 airfoils pitched about their quarter chord span axes from zero to sixty degrees incidence. The models were pitched at rates from 115 deg/sec to 1380 deg/sec at chord Reynolds numbers from 25,000 to 200,000 in accordance with the test matrix shown below. The numbers within the matrix indicate the associated non-dimensional pitch rate, α^+.

Table 1
Test Matrix

$\dot\alpha$(deg/sec)	115	230	460	920	1380
U_∞ (ft/sec)					
10	0.1	0.2	0.4	0.8	1.2
20		0.1	0.2	0.4	0.6
30					0.4
40			0.1	0.2	
60			0.067		0.2
80			0.05	0.1	

Five essentially identical models were used for three experimental techniques employed to examine the flowfield about the pitching airfoils. The experiments performed were smoke-wire flow visualization to obtain insight into the dynamics of the flowfields, dynamic surface pressure measurements to determine the transient aerodynamic loads, and near-surface hot-film velocity magnitude measurements in an attempt to understand the relative strengths of the passing vortices.

The flow visualization airfoil was painted flat black to reduce reflections from the surface when illuminated by high intensity strobe lights. The "smoke-wire" was a four-chord length of 0.005 in. tungsten wire placed two chords upstream of the airfoil leading edge in order to produce a fine planar sheet of streaklines in the flow normal to the airfoil span. The "smoke sheet" was produced by vaporizing Roscoe theatrical fog fluid coated onto the wire. The strobe lights were synchronized to a Redlakes

---

* Chief, Aerospace Mechanics Div, Member AIAA
** Professor of Mech Engineering, Member, AIAA

Locam II 16 mm high speed motion picture camera operating at 200 frames/sec for data recording.

The pressure airfoil was instrumented with 18 Endevco 8507-2 miniature pressure transducers close-coupled to a single airfoil surface. This effectively provided 36 pressure locations on the airfoil surface by pitching the airfoil up for the upper surface data set then down for the lower. Each pressure port was sequentially sampled 200 times over the sample period (determined by the start of the airfoil motion and the greater of either the time of the airfoil motion or the time for downstream convection of the dynamic stall vortex), and an ensemble average ·of 25 repetitions of each event was taken.

The near-surface velocity magnitude measurement models consisted of three airfoils with seven single element .hot-film probes protruding from each of the airfoil surfaces at heights of 0.017c, 0.033c, and 0.05c. While the pressure transducers were placed at a constant span location, the hot-film elements were offset to preclude wake interactions with trailing probes. Velocity magnitude data was taken in a fashion similar to the pressure data. Further information on the instrumentation and data acquisition system can be found elsewhere.[11,14,15]

Because of the massive amount of data acquired in performing the experiments in the test matrix of Table 1, only a few select cases can be presented. These are shown in Table 2.

Table 2

Case	U_∞(ft/sec)	Re	$\dot{\alpha}$(deg/sec)	α^+
I	10	25000	115	0.1
II	10	25000	230	0.2
III	20	50000	230	0.1
IV	20	50000	460	0.2
V	40	100000	460	0.1
VI	40	100000	920	0.2
VII	80	200000	920	0.1
VIII	60	150000	1380	0.2

Results

Previous studies [11,14,16] have presented some information on the nature of the unsteady vortex dominated flowfields about airfoils pitching at high rates to high angles of attack through flow visualization; others [10,12,14,17] have presented quantitative information on the large aerodynamic forces produced by these types of flowfields; and some [11,16] have provided near surface velocity information. The present study shows that all three techniques can be correlated due to the repeatability of the airfoil motions and resultant dynamic stall vortex structures. In addition, it shows that the flowfields are governed by the non-dimensional pitch rate, α^+, while being relatively Reynolds number independent. Cook[18] has provided a theoretical basis for the latter result by showing that, for inertia force dominated flows, the non-dimensional pitch rate - introduced through the boundary conditions rather than the momentum equations themselves - can provide effects that are orders of magnitude greater than Reynolds number effects.

Flow Visualization

Flow visualization techniques can provide the researcher with a great deal of information about the flowfields of interest. They can also aid in the selection and placement of sensors for quantitative data. The smoke-wire technique is, however, limited to low flow speeds, a drawback for Reynolds number dependent flows. In addition, it produces streaklines which can be ambiguous in still photography since streaklines are not coincident with streamlines in unsteady flows.

From the test matrix in Table 1, flow visualization studies were performed on all cases for freestream velocities of 10 and 20 ft/sec. Four of these are presented as Cases I, II, III, and IV shown in Table 2.

Figures 1,2,3, and 4 are for Cases I, II, III, and IV respectively. Figures 1 and 2 show single event sequences of flow over the airfoil as it pitches up in angle of attack from zero to sixty degrees in five degree increments in frames A-M. Frames N and O show the airfoil at sixty degrees angle of attack for an additional two equal time increments beyond the airfoil motion. Figures 3 and 4 show the airfoil in 10 degree increments as it pitches to sixty degrees angle of attack beginning at 10 degrees. In each case, flow is from left to right, and the airfoil pitches in a clockwise (cw) manner.

As airfoil rotation begins in Figure 1A and continued through Figure 1D for Case I, the flow transitions from a state of quasi-steady flow with symmetric alternating vortices shed into the wake to that of an asymmetric forced unsteady flow. An increasing number of apparently stronger vortices of counterclockwise (ccw) sense are shed from the lower airfoil surface with a concomitant decrease in number and strength of shed vortices of cw sense. This is accompanied by a movement from the trailing edge forward of a separation zone on the upper surface. As this separation zone grows, it appears that a shear layer interaction between the inviscid outer flow and the viscous boundary layer region produces a recirculation region. Within this region a number of small laminar vortical structures of cw sense occur. These small coherent structures do not last long however. Between angles of attack of 15 and 20 degrees shown in Figures 1D and 1E, they have been absorbed into the turbulent layer which has formed and moved forward from the trailing edge. During this same interval, what would appear in quasi-steady flow to be a laminar separation bubble has formed near the leading edge.

But this is clearly not a separation bubble in the classic sense. By an airfoil angle of attack of 25 degrees in Figure 1F, it is obvious that a cw rotating vortex has formed. At the point of initiation of this dynamic stall vortex, there appears to be a decided diminution of the ccw vortices being shed into the wake from the lower surface. The dynamic stall vortex continues to grow while remaining attached to the

airfoil until an angle of attack of slightly less than 35 degrees, at which point in Figure 1H it can be seen to have separated. As it begins to convect downstream – at approximately 30% of the freestream velocity – no ccw vortex shedding from the lower surface can be observed. By an airfoil angle of attack of 40 degrees in Figure 1I, however, with the dynamic stall vortex fully separated from the airfoil, the beginnings of the formation of a large ccw vortex can be seen aft of the trailing edge. This continues to 55 degrees in Figure 1L. Following this, the ccw vortex sheds into the wake and another cw vortex forms over the upper surface. Both of these latter vortices are more coherent than those formed by bluff body shedding in unforced unsteady flows.

Case III, shown in Figure 3, duplicates the non-dimensional pitch rate of 0.1 in Case I; however, both pitch rate and freestream velocity have been doubled. As in Case I, at 10 degrees angle of attack in Figure 3A, vortices of ccw sense can be observed shedding from the lower surface while a relatively thin upper surface separation zone moves from the trailing edge forward. By 20 degrees in Figure 3B, dynamic stall vortex initiation is evident near the leading edge. At 30 degrees, the vortex has grown to one-half chord in diameter – the size of the vortex being defined as merely that which can be conveniently measured by the observer. The dynamic stall vortex has clearly separated from the airfoil by an angle of attack of 40 degrees in Figure 3D, with the beginnings of a new ccw vortex being formed aft of the trailing edge and growing through an airfoil angle of attack of 50 degrees in Figure 3E. The initiation and growth of the dynamic stall vortex and, with minor exceptions, the rest of the flowfield for this case is virtually identical to Case I. These differences are the thicknesses of the separated regions on the upper surface prior to dynamic stall vortex initiation and the laminar vortex structures within the recirculation zone evident in Case I.

Case II is a flowfield generated by the airfoil pitching at twice the rate of that in Case I, but at the same Reynolds number for a non-dimensional pitch rate of 0.2. Many similarities exist between Case I and II with respect to the genesis and evolution of the dynamic stall vortices, so it is perhaps more illuminating to point out the differences. As the airfoil pitches up to 30 degrees angle of attack in Figure 2F, the movement of the upper surface separation point, the formation of the recirculation zone, and the initiation of the dynamic stall vortex are all delayed by approximately five degrees in angle of attack beyond those in Case I. In addition, the ccw vortices shed from the lower surface have undergone increased rotation. As the dynamic stall vortex grows at the higher non-dimensional pitch rate, it retains its curvature and coherence and remains attached to the airfoil at higher angles of attack. It separates from the airfoil at an angle of attack between 50 and 55 degrees shown in Figures 2K and 2L – more than 15 degrees beyond that of Case I. Finally, once the vortex sheds from the upper surface of the

airfoil, it convects downstream somewhat more rapidly at 40% of the freestream velocity.

Case IV is also at a non-dimensional pitch rate of 0.2, achieved by doubling both pitch rate and freestream velocity of Case II. The same conclusions can be drawn when comparing Case IV to Case II as when comparing Cases III to Case I. The flowfields as functions of angle of attack are virtually identical – the exceptions being that for the higher Reynolds number case, the upper surface separated region is thinner and more turbulent. This precludes the identification of the small scale cw vortex structures in the recirculation zone.

Pressure Measurements

Dynamic surface pressure measurements provide for quantitative analysis of the aerodynamic forces on the airfoil resulting from the unsteady driven flow. Temporal pressure, lift, pressure drag, and quarter-chord moments can be calculated from these data. Pressure data over the surface of the airfoil were taken for all cases in the test matrix of Table 1; however, for this report we will limit discussion to values of the non-dimensional pitch rate of 0.1 and 0.2 as in the flow visualization analysis. Further, while pressure measurements at a freestream velocity of 10 ft/sec showed consistent trends, signal to noise was so low that the measurements were unreliable. The cases presented are, therefore, at freestream flow velocities of 20 ft/sec and greater, shown as Cases III through VIII in Table 2. Note that Cases III and IV are two of those examined in the flow visualization section.

Conventional plots of two-dimensional pressure coefficients versus non-dimensional chord at given angles of attack are inadequate to communicate enough detail, succinctly, for the reader to understand the complete effects of these time-dependent flowfields. For this reason, two-dimensional representations of three-dimensional carpet plots of pressure coefficient ($-C_p$) vs non-dimensional chord (x/c) vs angle of attack (alpha) have been generated. Figures 5A and 5B show results for the upper and lower surfaces of the airfoil, respectively, for Case V. The x,y, and z axes are non-dimensional chord length from leading to trailing edge, alpha from 0 to 60 degrees, and negative C_p, respectively.

Lower surface pressure distributions shown in Figure 5B produced no surprises. The results are not too dissimilar to what one would expect in steady flow. The upper surface in Figure 5A, on the other hand, shows dramatic changes in pressure coefficient over the airfoil chord as a function of angle of attack. As the airfoil pitches up to greater than 20 degrees angle of attack, the negative C_p at the leading edge grows very large with a slight hesitation from about 12 to 14 degrees. From flow visualization, Figures 1C to 1D, this hesitation appears to be in the angle of attack range at which the upper surface separation zone approaches the leading edge. At about 22 degrees the leading edge suction peak reaches a maximum and begins to drop off. From Figures 1E and 1F and Figure 3B, this is the point at which the dynamic stall vortex is

formed. At approximately 28 degrees angle of attack, pressure coefficient reaches its maximum negative value at a position slightly aft of the quarter-chord. These two peaks produce a saddle shaped region in the plot. The pressure peak then begins to diminish and move aft over the airfoil as angle of attack continues to increase. From 38 to 44 degrees, C_p is relatively low over the entire chord forming a valley with respect to angle of attack. Then from 48 to 60 degrees, first the region near the trailing edge and then the region near the leading edge undergo large negative increases in C_p. From Figures 1J to 1M and Figures 3E to 3F, this corresponds to the large induced vortices formed after shedding of the dynamic stall vortex.

From flow visualization evidence, it was asserted that the non-dimensional pitch rate was the parameter of primary ·importance for similarity of these forced unsteady flowfields. Figures 6, 7, and 8 are quantitative evidence supporting this hypothesis. They are plots of C_p vs chord for selected angles of attack for Cases V, III, and VII, respectively. These show a high degree of similarity in shape and magnitude of temporal pressure coefficient distributions among flowfields generated with over a factor of four difference in pitch rate and freestream velocities.

Integrating the pressure coefficients yields the aerodynamic coefficients of lift (C_ℓ), pressure drag (C_d), and quarter-chord moment ($C_{mc/4}$). Figures 9, 10, and 11 show C_ℓ vs alpha, C_d vs C_ℓ, and $C_{mc/4}$ vs alpha, respectively, for the $\alpha^+ = 0.1$ cases III, V, and VII overlaid for comparison. For each of these cases, as the airfoil pitches up, lift coefficient rises at a rate slightly higher than 0.1/deg for the first few degrees of rotation. The slope is then depressed to about 0.06/deg until C_ℓ reaches its peak value of between 2.1 and 2.4 at an angle of attack between 30 and 32 degrees. Comparing this with the flow visualization, Figures 1G and 1H, this appears to be the point at which the dynamic stall vortex separates from the airfoil. Lift coefficient then drops rapidly to a value of 1.1 and remains so until undergoing a rise to 1.5 beginning at 46 to 48 degrees. This rise closely coincides with the secondary induced vortices observed in Figures 1K through 1M. For a steady flow comparison[15], at these low Reynolds numbers, peak lift coefficients fall between 0.8 and 0.85 at angles of attack of 12.0 to 12.5 degrees.

As one might expect, drag becomes quite large as lift increases beyond the maximum steady flow values. Note that the drag coefficient actually decreases for some time after the dynamic stall vortex separates. Pitching moment exhibits a relatively low, but increasingly negative trend until vortex separation, at which time the airfoil undergoes a sharp pitch down moment.

At the higher non-dimensional pitch rate of 0.2, the carpet plot of $-C_p$ vs x/c vs alpha is shown in Figure 12A and 12B for Case VI. While the general shape of this temporal pressure surface is similar in nature to that of Case V in Figures 5A and 5B, there are significant differences between upper surface plots. The dramatic increase in negative C_p at the leading edge is delayed approximately five degrees in angle of incidence beyond those of lower α^+ values. There is also no hesitation in its increase to larger magnitudes for the leading edge suction peak. The saddle produced between this peak and the one corresponding to passage of the dynamic stall vortex from flow visualization in Figures 2F through 2H indicates transformation to the dynamic stall vortex is more pronounced. The maximum pressure peak occurring while the vortex is resident over the airfoil is nearly one and one-half times as large as for the lower non-dimensional pitch rate. For motion up to 60 degrees angle of attack, no secondary pressure peaks were observed. The two-dimensional $-C_p$ vs x/c plots in Figures 13, 14, and 15 show the large pressure peaks associated with these forced unsteady flows for Cases VI, IV, and VIII, and, additionally, the similarities for constant values of α^+.

As in the lower α^+ cases, the lift curve in Figure 16 shows a relatively high slope for the first six to eight degrees of rotation and then a depressed slope of about 0.06/deg up to peak values of C_ℓ between 2.4 and 3.2. $C_{\ell\,max}$ occurs between 35 to 45 degrees, but there is no subsequent sharp drop in lift coefficient. Drag in Figure 17 for these cases is quite high and also decreases with angle of attack beyond that for $C_{\ell max}$. Figure 18 shows moment coefficient data exhibiting low, decreasing values until the point at which $C_{\ell\,max}$ is reached, at which time its slope becomes more negative.

Near-Surface Velocities

Near-surface velocity magnitude measurements - particularly when correlated with flow visualization - can provide an insight into the flow immediately surrounding the airfoil. Since single element hot-film sensors were used for these measurements, only the magnitude of the velocity component normal to the sensor can be measured. Since the flows of interest have been shown[15] to be two-dimensional during airfoil rotation, and since the sensors have been placed in close proximity to the airfoil surface, it was assumed that the measured flow speed is the positive or negative u component of velocity. It was anticipated that this would be an excellent assumption for the lower sensor heights and less so for the higher one, but then only when relatively low speed flow was directed in toward the airfoil surface. With this caveat, velocity magnitudes were taken for each of the cases in Table 1. For the purposes of this report only that of Case V will be discussed in detail.

For the same reasons as for the pressure measurements, data is presented in carpet plots of velocity magnitude vs chord vs alpha corresponding to the z, x, and y axes, respectively. Figures 19A and 19B, Figures 20A and 20B, and Figures 21A and 21B show flow speeds above the upper and lower surfaces at 0.1, 0.2, and 0.3 inches, respectively.

The lower surface measurements exhibit nothing out of the ordinary with the exception of an unusually low velocity reading near the

trailing edge at high angles of attack obtained from the 0.3 in. sensors. The upper surface measurements track, in phase and relative magnitudes, the results from the pressure data. In Figure 19A, the rapid rise to the suction peak near the leading edge is consistent with Figure 5A, even to the hesitation from 10 to 12 degrees angle of attack. Once the flow speed reaches its peak at an alpha of 18 to 20 degrees, it drops rapidly. Comparing this with the flow visualization in Figure 1E, this corresponds to the point at which the dynamic stall vortex initiates. There is no saddle shaped transformation from the leading edge suction peak to the dynamic stall vortex peak as in the pressure measurements since the pressure transducers are not sensing similar changes in velocity the hot-film gauges are, but rather, are integrating continuously through the boundary layer. The velocity magnitude then climbs rapidly back to another peak which forms a diagonal ridge from leading to trailing edge with increasing alpha. This ridge is then followed by a valley in the plot along the airfoil chord, and subsequently, by the trailing and leading edge peaks comparable to those in Figure 5A. Figures 20A and 21A for sensor heights of 0.1 and 0.2 inches show similar results except for the relative magnitudes.

Figures 22A and 22B show velocity magnitudes at sensor heights of 0.1 inches above the airfoil surface for the non-dimensional pitch rate of 0.2 for Case VI. This shows equal consistency with the pressure data from Figure 12A as those sets described above for the lower α^+ value.

Discussion

Airfoils pitching at high rates to high angles of attack produce coherent, repeatable, and energetic dynamic stall vortices over the suction surfaces of the airfoils. These vortices result in large transient aerodynamic forces on the airfoils which are increasing functions of the non-dimensional pitch rate. These aerodynamic forces have been quantified by dynamic surface pressure measurements and corroborated by the near-surface velocity magnitude measurements. Flow visualization has been used to interpret the results of both the pressure and velocity measurements. This can be readily done because of the dynamic similarity of the flowfields for constant values of the non-dimensional pitch rate.

From the flow visualization data, it appears that, as the airfoil pitches up, a large amount of ccw (from our perspective) vorticity is shed into the wake through a series of vortices leaving the lower surface. A steady flow analogy would be a series of starting vortices. This results in a commensurate accumulation of cw vorticity around the airfoil. This explanation is similar in nature to that of Reynolds and Carr[2], but from a slightly different perspective. The initiation of the dynamic stall vortex does not appear to directly affect this vorticity accumulation so long as it remains attached or bound to the airfoil. During this time the dynamic stall vortex grows and appears to gain strength while being fed energy by the external flow. After it separates and begins to

convect downstream, it appears to grow and dissipate as a free vortex. While the flowfields remain fundamentally similar for constant α^+ over a fairly wide range of Reynolds numbers, there do appear to be some Reynolds number effects. At the higher Reynolds numbers the separated region over the upper surface is thinner, and the attendant recirculation region is less well defined. There also appears to be more turbulence in the wake and less well defined shedding vortices. Much larger variations are, however, noted for changes in non-dimensional pitch rate. As α^+ increases, the initiation of the dynamic stall vortex is delayed to higher angles of attack. The shedding of ccw vortices into the wake as the airfoil begins to pitch up is more pronounced. The dynamic stall vortex contains a larger amount of vorticity apparent from its greater curvature. It also remains attached to the airfoil for higher angles of attack before convecting downstream.

Pressure and hot-film data are in consonance and directly support the observations for flow visualization. Initiation of the dynamic stall vortex appears to be well defined. The position of the dynamic stall vortex as a function of airfoil angle of attack is readily evident due to its effect on surface pressures and near-surface velocities. The direction of the flow near the airfoil surface can even be determined and correlated as a function of angle of attack. Finally, for the lower non-dimensional pitch rate, the large secondary vortices induced over the upper surface by the passage of the dynamic stall vortex have been quantified.

Conclusions

These experiments were conducted to determine the nature of the flowfield about airfoils pitching at high constant rates to large angles of attack, to quantify the aerodynamic forces elicited by these motions, and to obtain some understanding of the velocity field in close proximity to the airfoil. As the airfoil pitches up, a dynamic stall vortex forms near the leading edge and is the dominant characteristic of the flowfield. Large transient aerodynamic forces were measured; e.g., lift coefficients greater than four times the maximum steady flow value. While the dynamic stall vortex has a great deal of influence on the temporal and spatial values of these large aerodynamic forces, the forces are not generated by the dynamic stall vortex, per se; but rather by the accumulation of vorticity about the airfoil including the vortex itself.

A further objective of these experiments was to determine the effects of Reynolds number, pitch rate, and non-dimensional pitch rate on the flowfields. For these experiments, Reynolds number effects were limited to freestream velocity variations since the same chord was used on all models. It was found that Reynolds number and pitch rate, for constant values of non-dimensional pitch rate, had at most only second order effects on the flowfields. The non-dimensional pitch rate, α^+, proved to be the determining factor over a wide range of flow velocities and pitch rates, providing dynamic similarity among flowfields.

References

1. McCroskey, W.J., "Unsteady Airfoils," Annual Review of Fluid Mechanics, pp. 285-311, 1982.
2. Reynolds, W.C., and Carr, L.W., "Review of Unsteady, Driven, Separated Flows," AIAA-85-0527, AIAA Shear Flow Cont. Conf., 12-14 Mar 1985, Boulder, CO.
3. Ham, N.D., and Garelick, M.S., "Dynamic Stall Considerations in Helicopter Rotors," J. AM. Hel. Soc., Vol. 13, No. 2, pp. 40-50, Apr 1968.
4. McCroskey, W.J., and Philippe, J.J., "Unsteady Viscous Flow on Oscillating Airfoils," AIAA J., Vol. 13, No. 1, pp. 71-79, Jan 1975.
5. McAlister, K.W., and Carr, L.W., "Water Tunnel Visualization of Dynamic Stall," J. Fluids Engr., Vol. 101, pp. 376-380, Sep 1978.
6. Robinson, M.C., and Luttges, M.W., "Unsteady Separated Flow: Forced and Common Vorticity About Oscillating Airfoils," Workshop on Unsteady Separated Flows, pp. 117-126, USAF Academy, 10-11 Aug 1983, published by the Univ. of CO Dept. of Aero. Engr. Sci.
7. Martin, J.M., Empey, R.W., McCroskey, W.J., and Caradonna, F.X., "An Experimental Analysis of Dynamic Stall on an Oscillating Airfoil," J. Am. Hel. Soc., Vol. 19, No. 1, pp. 26-32, Jan 1973.
8. Ericsson, L.E., and Reding, J.P., "Dynamic Stall Analysis in Light of Recent Numerical and Experimental Results," J. Aircraft, Vol. 13, No. 4, Apr 1976, pp. 248-255.
9. Carr, L.W., McAlister, K.W., and McCroskey, W.J., "Analysis of the Development of Dynamic Stall Based on Oscillating Airfoil Experiments," NASA TN D-8382, Jan 1977.
10. Francis, M.S., Keesee, J.E., and Retelle, J.P., "An Investigation of Airfoil Dynamic Stall with Large Amplitude Motions," FJSRL-TR-83-0010, Oct 1983.
11. Walker, J.M., Helin, H.E., and Strickland, J.H., "An Experimental Investigation of an Airfoil Undergoing Large Amplitude Pitching Motions," AIAA J., Vol. 23, No. 8, Aug 1985, pp. 1141-1142, also AIAA-85-0039, AIAA 23rd Aerospace Sci. Mtg., Reno, NV, Jan 1985.
12. Jumper, E.J., Schreck, S.J., and Dimmick, R.L., "Lift-Curve Characteristics for an Airfoil Pitching at Constant Rate," AIAA-86-0117, AIAA 24th Aerospace Sci. Mtg., 6-9 Jan 1986, Reno, NV.
13. Strickland, J.H., and Graham, G.M., "Force Coefficients for a NACA-0015 Airfoil Undergoing Constant Pitch Rate Motions," AIAA J., Vol. 25, No. 4, Apr 1987, pp. 622-624.
14. Walker, J.M., Helin, H.E., and Chou, D.C., "Unsteady Surface Pressure Measurements on a Pitching Airfoil," AIAA-85-0532, AIAA Shear Flow Cont. Conf., 12-14 Mar 1985, Boulder, CO.
15. Walker, J.M., "Forced Unsteady Vortex Flows Driven by Pitching Airfoils," FJSRL-TR-86-0010, Oct 1986.
16. Helin, H.E., and Walker, J.M., "Interrelated Effects of Pitch Rate and Pivot Point on Airfoil Dynamic Stall," AIAA-85-0130, AIAA 23rd Aerospace Sci. Conf., Reno, NV, Jan 1985.
17. Francis, M.S., and Keesee, J.E., "Airfoil Dynamic Stall Performance with Large-Amplitude Motions," AIAA J., Vol. 23, No. 11, Nov 1985, pp. 1653-1659.
18. Cook, R.J., "Similarity Conditions for Flows About Pitching Airfoils," FJSRL-TM-87-0003, Jun 1987.
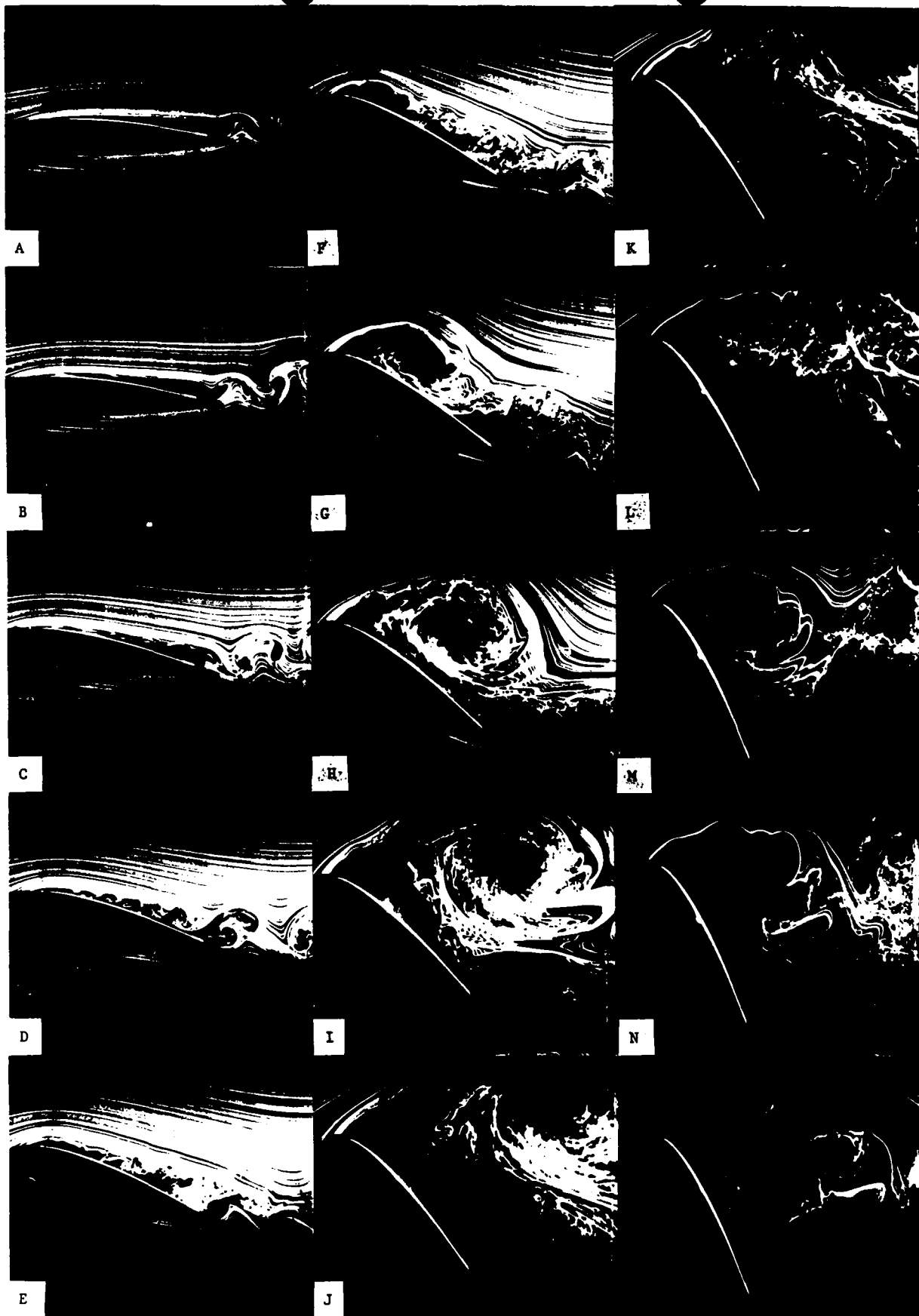
Figure 1. Flow Visualization, Case I
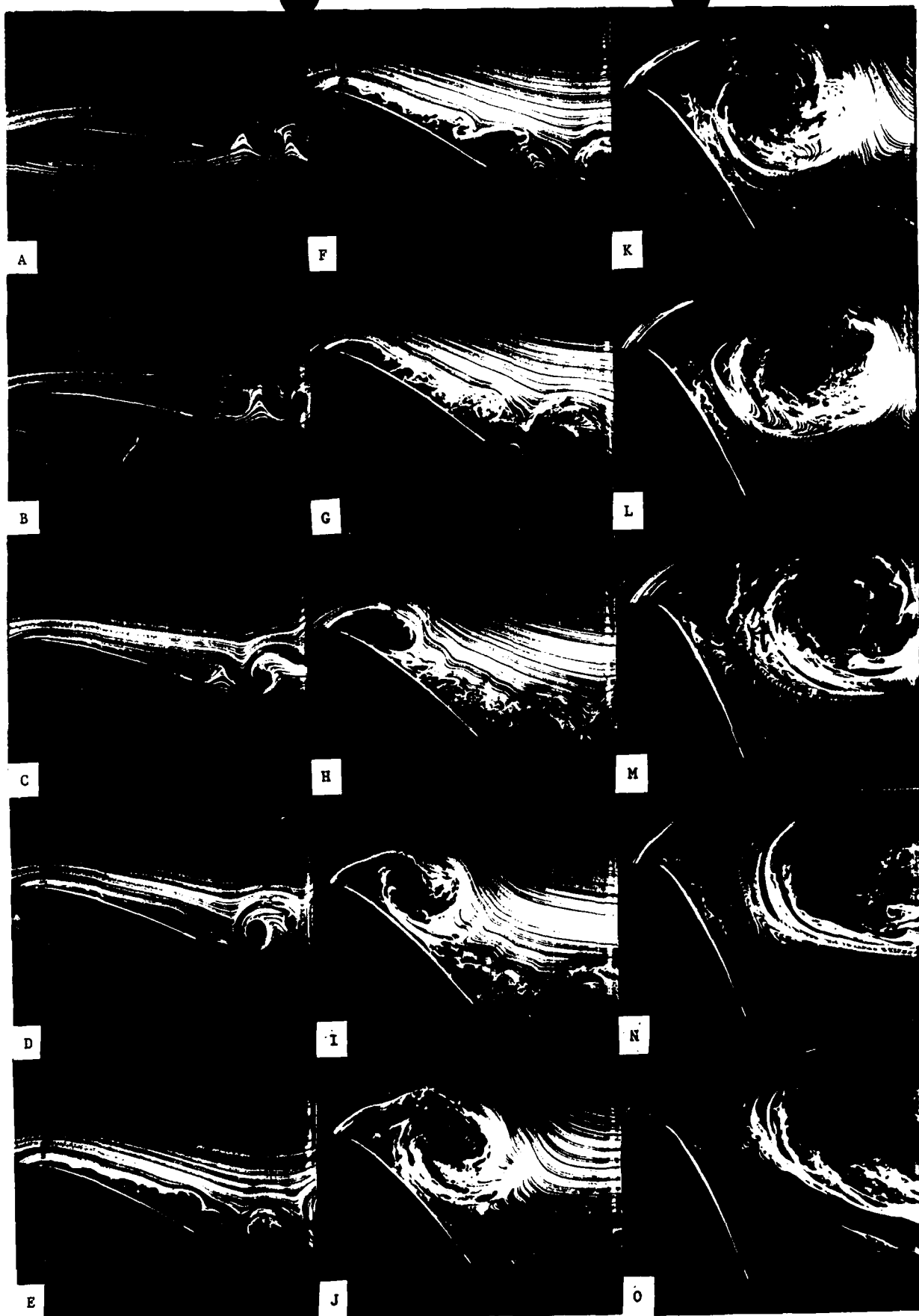
Figure 2. Flow Visualization, Case II

8
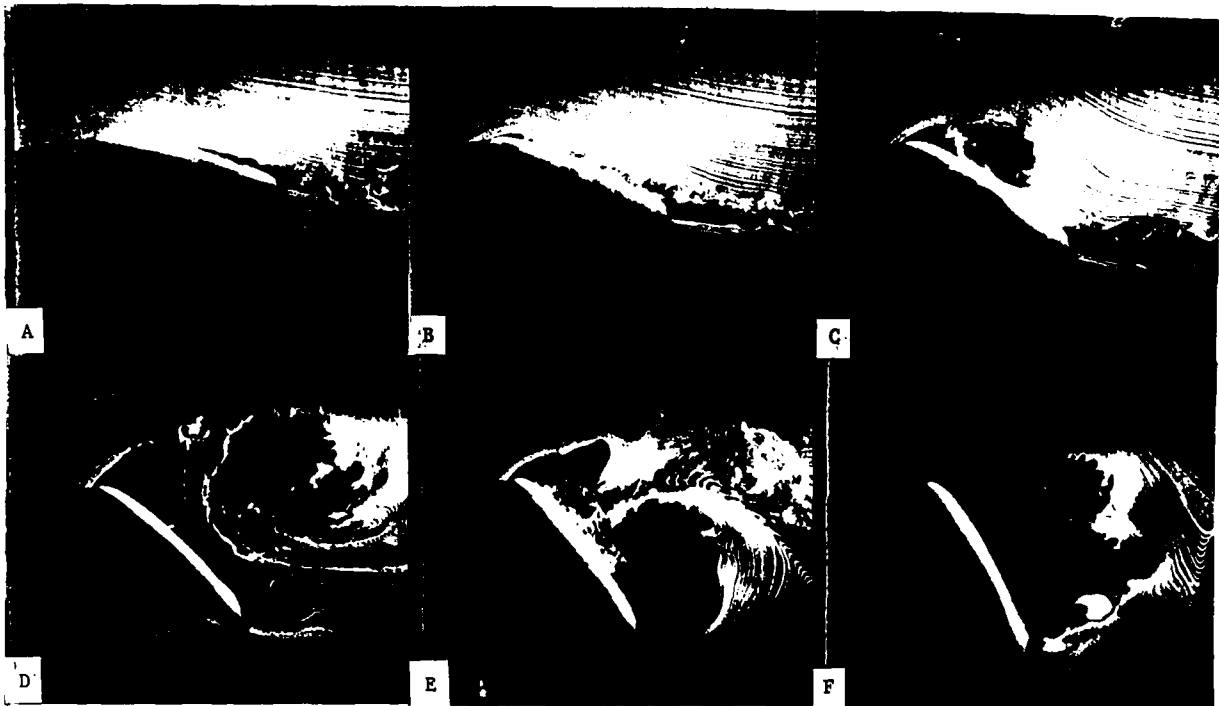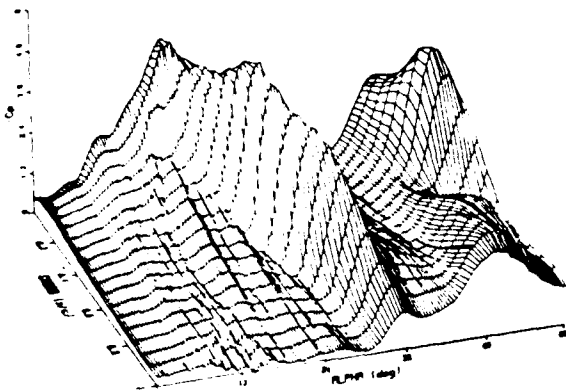
Figure 3. Flow Visualization, Case III
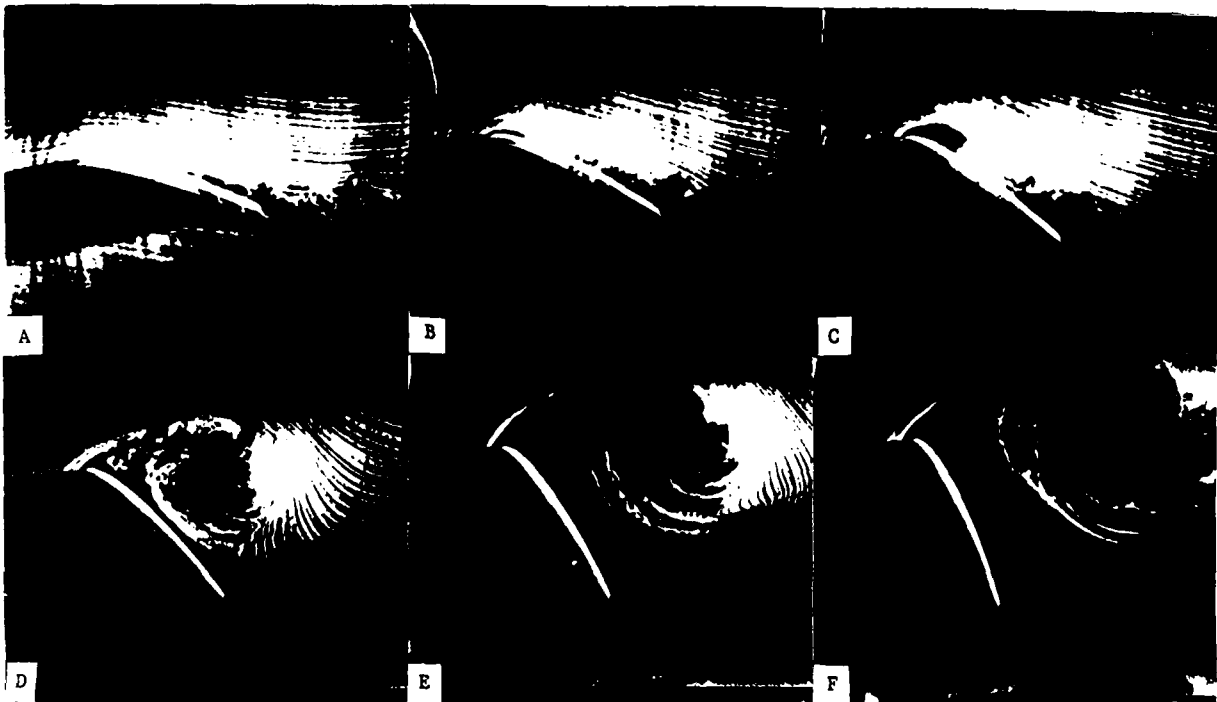
Figure 4. Flow Visualization, Case IV

9

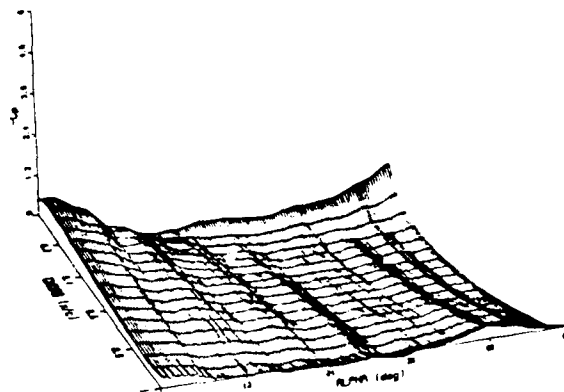Alpha+=0.1, PR=460d/s, U=40fps

Alpha+=0.1, PR=460d/s, U=40fps

Figure 5   Pressure Coefficient Map. Case V,
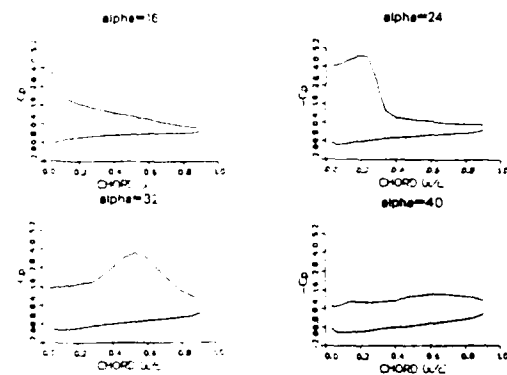A - Upper Surface, B - Lower Surface

Alpha+=0.1, PR=460d/s, U=40fps

alpha=16   alpha=24

alpha=32   alpha=40

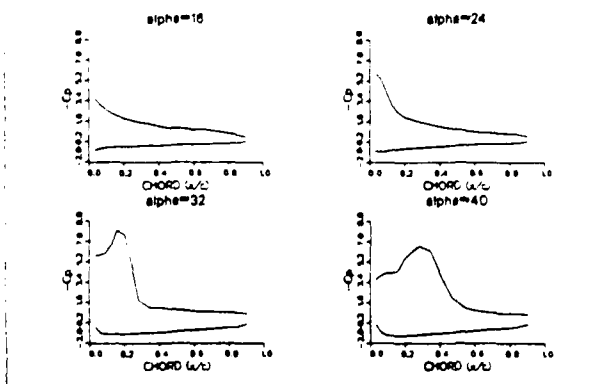Figure 6 C_p vs x/c. Case V

Alpha+=0.1, PR=230d/s, U=20fps

alpha=16   alpha=24

alpha=32   alpha=40
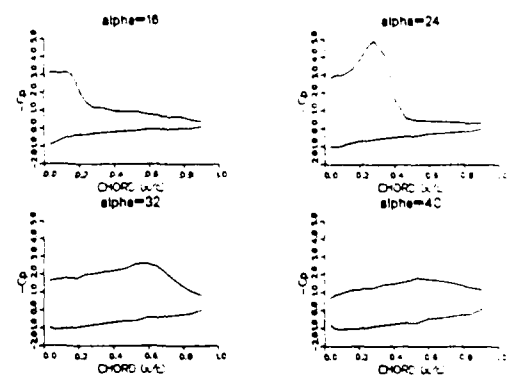
Figure 7 C_p vs x/c. Case III

Alpha+=0.1, PR=920d/s, U=80fps

alpha=16   alpha=24

alpha=32   alpha=40
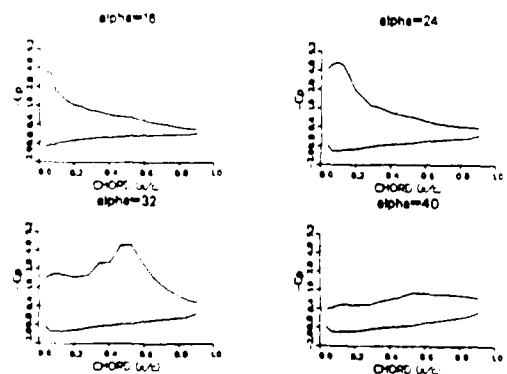
Figure 8 C_p vs x/c. Case VII

Alpha+=0.1
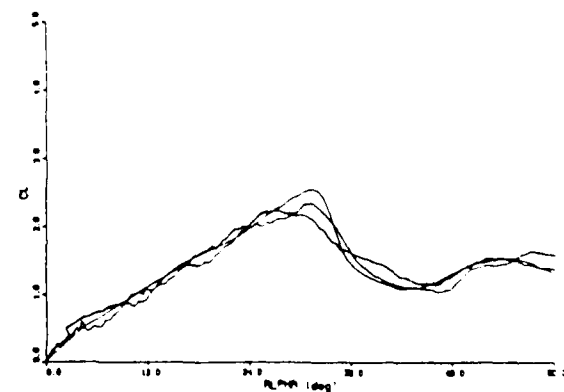
Figure 9 C_L vs alpha. Cases III, VI, VII
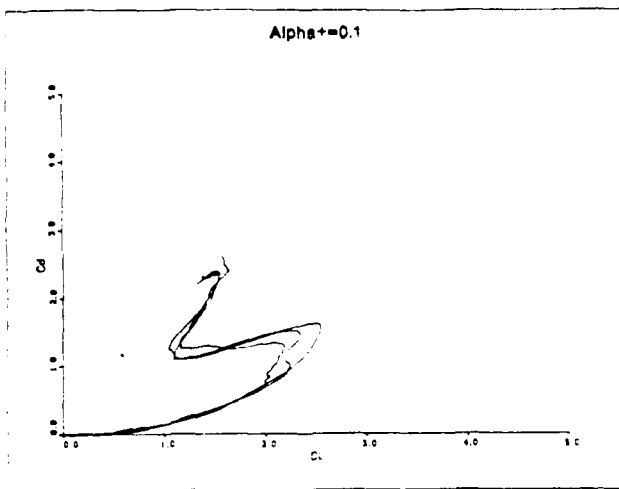
Alpha+=0.1

Figure 10 C_d vs C_1. Cases III, VI, VII
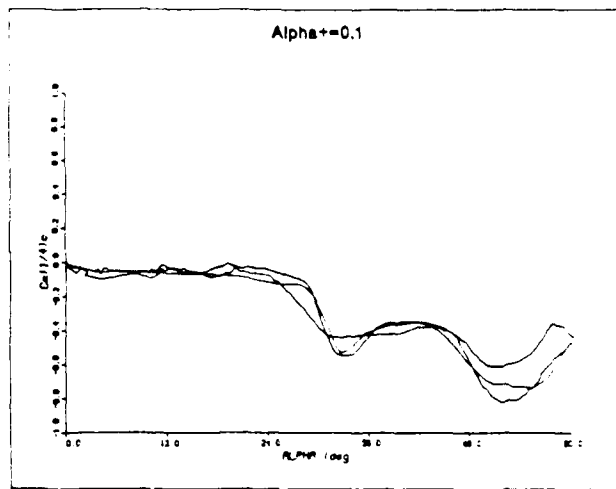
Alpha+=0.1

Figure 11 $C_{mc/4}$ vs alpha. Cases III, VI, VII

Alpha+=0.2, PR=920d/s, U=40fps
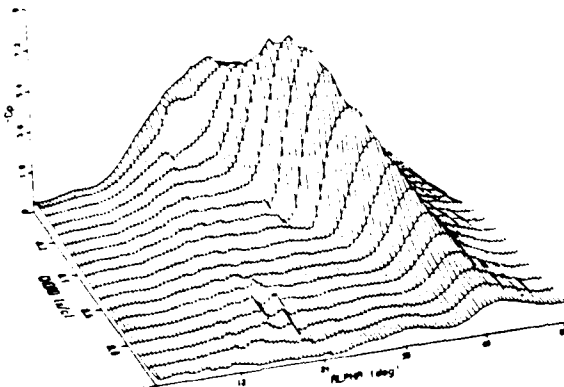
Alpha+=0.2, PR=920d/s, U=40fps
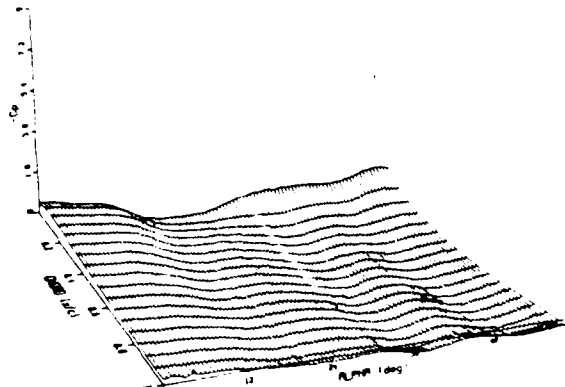
Figure 12   Pressure Coefficient Map. Case VI

A - Upper Surface, B - Lower Surface

Alpha+=0.2, PR=920d/s, U=40fps

alpha=16   alpha=24

alpha=32   alpha=40

Figure 13 C_p vs x/c. Case VI

Alpha+=0.2, PR=460d/s, U=20fps

alpha=16   alpha=24

alpha=32   alpha=40

Figure 14 C_p vs x/c. Case IV

11

Alpha+=0.2, PR=1380d/s, U=60fps
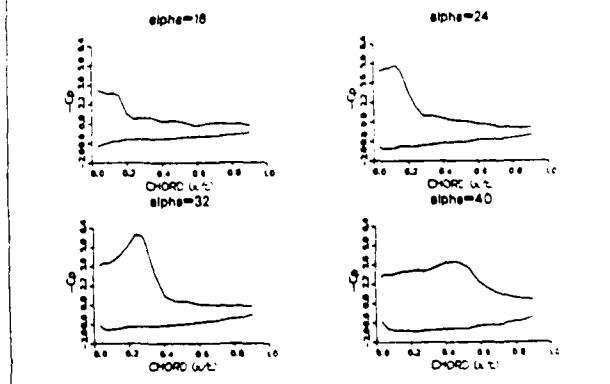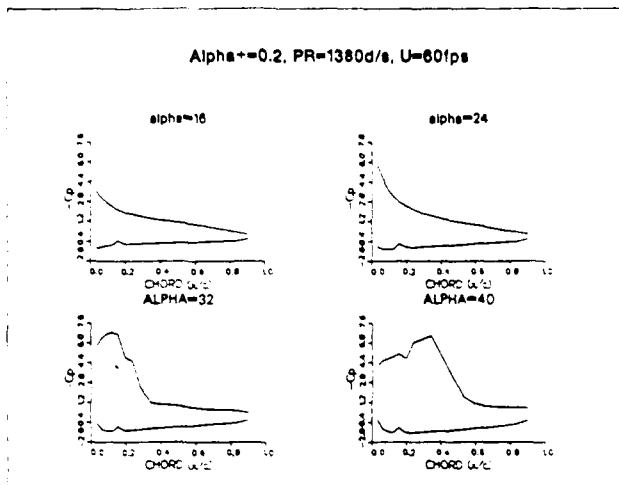
Figure 15 C_p vs x/c, Case VIII
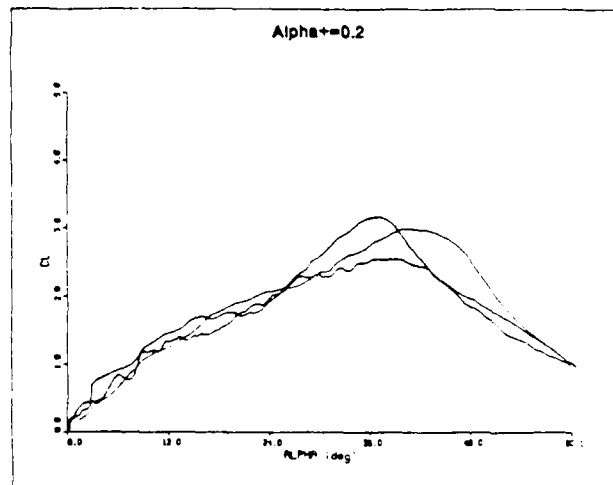
Alpha+=0.2

Figure 16 C_l vs alpha, Cases IV, VI, VIII
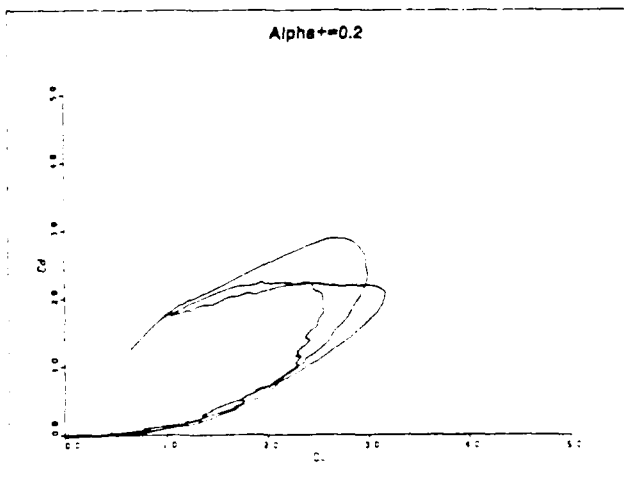
Alpha+=0.2

Figure 17 C_d vs C_l, Cases IV, VI, VIII
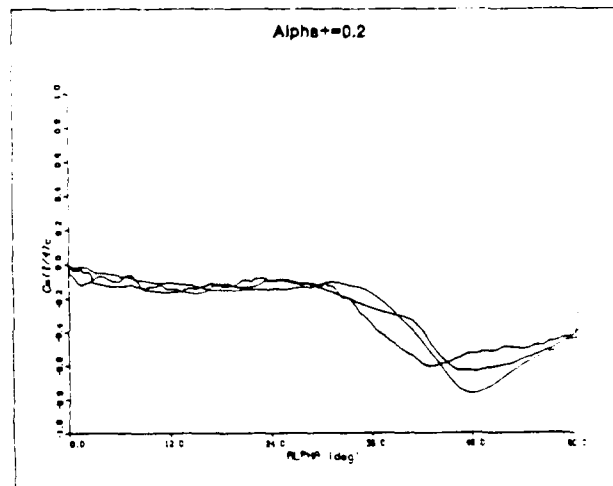
Alpha+=0.2

Figure 18 $C_{mc/4}$ vs alpha, Cases IV, VI, VIII

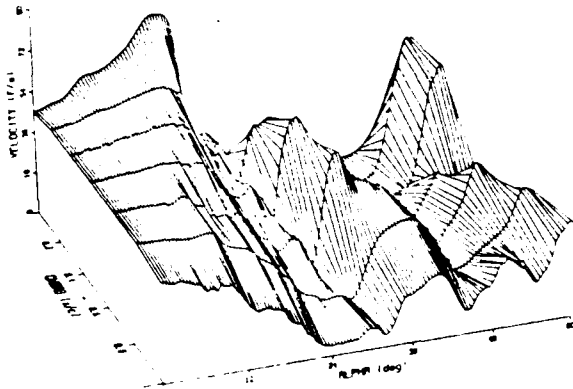Alpha+=0.1, 460/40, 0.1in.
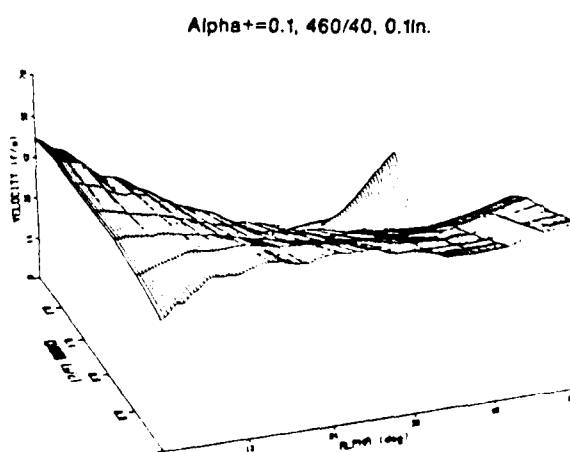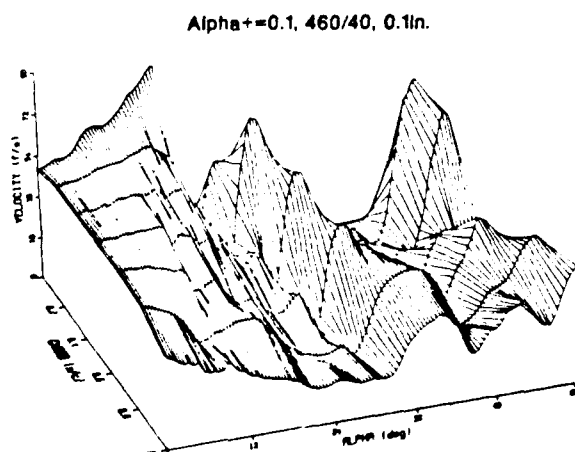
Alpha+=0.1, 460/40, 0.1in.

Figure 19 Near-Surface Velocity,
Sensor Height - 0.1 in., Case V
A - Upper Surface, B - Lower Surface
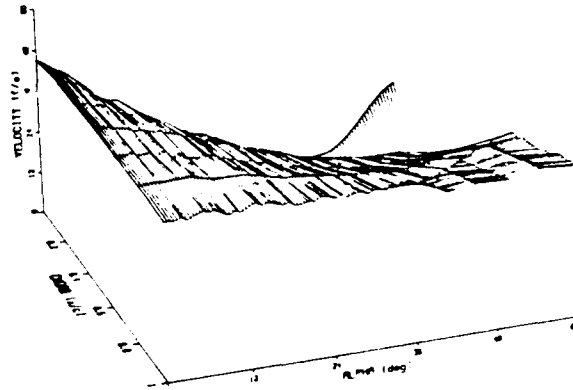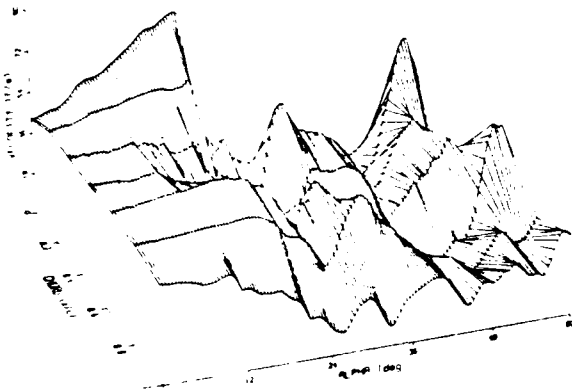
Alpha+=0.1, 460/40, 0.2in.

Alpha+=0.1, 460/40, 0.2in.

Figure 20. Bear-Surface Velocity.

Sensor Height = 0.2 in., Case V

A - Upper Surface, B - Lower Surface

Alpha+=0.1, 460/40, 0.3in.
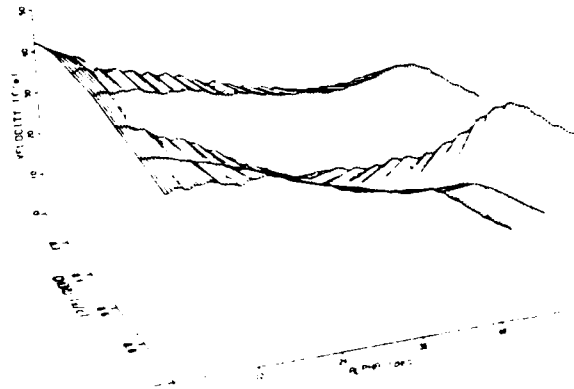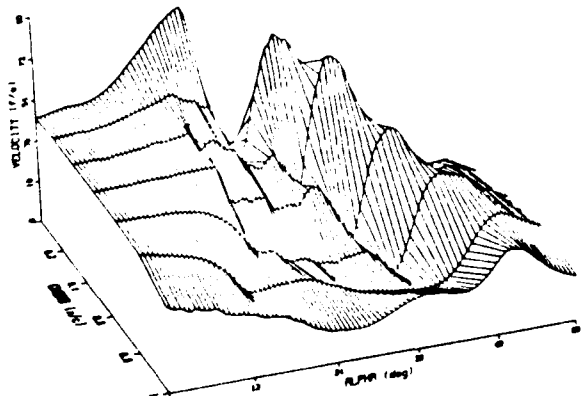

Alpha+=0.1, 460/40, 0.3in.

Figure 21. Bear-Surface Velocity.

Sensor Height = 0.3 in., Case V

A - Upper Surface, B - Lower Surface

Alpha+=0.2, 920/40, 0.1in.

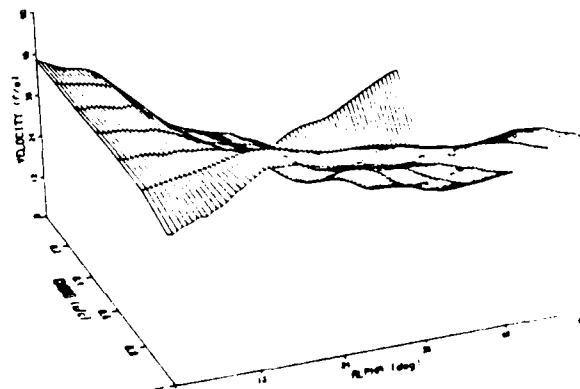
Alpha+=0.2, 920/40, 0.1in.

Figure 22. Bear-Surface Velocity.

Sensor Height = 0.1 in., Case VI

A - Upper Surface, B - Lower Surface

13